Article

Deformation Characteristic and Constitutive Modeling of 2707 Hyper Duplex Stainless Steel under Hot Compression

Huabing Li [1,*]**, Weichao Jiao** [1]**, Hao Feng** [1,*]**, Xinxu Li** [1]**, Zhouhua Jiang** [1]**, Guoping Li** [2]**, Lixin Wang** [2]**, Guangwei Fan** [2] **and Peide Han** [3]

[1] School of Metallurgy, Northeastern University, Shenyang 110819, China; jiaowcneu@163.com (W.J.); lxx20110180@163.com (X.L.); jiangzh@smm.neu.edu.cn (Z.J.)
[2] Technology Center of Taiyuan Iron and Steel Croup Co. Ltd., Taiyuan 030001, China; ligp@tisco.com.cn (G.L.); wanglx@tisco.com.cn (L.W.); fangw@tisco.com.cn (G.F.)
[3] College of Materials Science and Engineering, Taiyuan University of Technology, Taiyuan 030024, China; hanpeide@126.com
* Correspondence: lihb@smm.neu.edu.cn (H.L.); fenghao241@163.com (H.F.); Tel.: +86-24-8368-9580 (H.L. & H.F.); Fax: +86-24-2389-0559 (H.L. & H.F.)

Abstract: Hot deformation behavior and microstructure evolution of 2707 hyper duplex stainless steel (HDSS) were investigated through hot compression tests in the temperature range of 900–1250 °C and strain rate range of 0.01–10 s^{-1}. The results showed that the flow behavior strongly depended on strain rate and temperature, and flow stress increased with increasing strain rate and decreasing temperature. At lower temperatures, many precipitates appeared in ferrite and distributed along the deformation direction, which could restrain processing of discontinuous dynamic recrystallization (DRX) because of pinning grain boundaries. When the temperature increased to 1150 °C, the leading softening behaviors were dynamic recovery (DRV) in ferrite and discontinuous DRX in austenite. When the temperature reached 1250 °C, softening behavior was mainly DRV in ferrite. The increase of strain rate was conducive to the occurrence of discontinuous DRX in austenite. A constitutive equation at peak strain was established and the results indicated that 2707 HDSS had a higher Q value (569.279 kJ·mol^{-1}) than other traditional duplex stainless steels due to higher content of Cr, Mo, Ni, and N. Constitutive modeling considering strain was developed to model the hot deformation behavior of 2707 HDSS more accurately, and the correlation coefficient and average absolute relative error were 0.992 and 5.22%, respectively.

Keywords: 2707 hyper duplex stainless steel; hot deformation behavior; hot compression; microstructure; constitutive modeling

---

1. Introduction

Duplex stainless steel (DSS) with approximately equal volume fractions of ferrite (α) and austenite (γ) phases exhibits a good combination of mechanical properties and corrosion resistance. For this reason, DSSs are considered an excellent choice in various industrial applications, particularly in the oil and gas industry, petrochemical, and chemical processing [1–3]. With the development of industry, the requirement for the performance of DSSs becomes higher. 2707 hyper duplex stainless steel (HDSS) is a special class of DSS that contains high levels of Cr, Mo, Ni, and N, contributing to its excellent mechanical properties and a high value (45–50) of pitting resistance equivalent number (PREN) [4]. Therefore, 2707 HDSS can extend the application range of DSS into even more aggressive conditions [5].

However, the coexistence of austenite and ferrite with different deformation responses in these alloys makes the hot processing complicated [6].

Hot working is an important step in producing DSSs. It is known that ferrite is characterized by high stacking fault energy (SFE) and, therefore, undergoes dynamic recovery (DRV). On the contrary, austenite, having low SFE, undergoes only limited DRV, and dynamic recrystallization (DRX) comes into operation when the dislocation density reaches a critical value [7–10]. In this respect, the incoherence containing thermal expansion coefficient and flow response mechanism between the two constituents easily reduces hot workability of DSSs and then leads to the formation of defects on the surface of products [11]. Moreover, higher alloy content than traditional DSSs and higher sensitivity of secondary phase precipitation in the hot deformation process of 2707 HDSS further increase its processing difficulty. Therefore, it is necessary to investigate the hot deformation behavior of 2707 HDSS.

High temperature flow behavior, as the macro-reflection of the mechanisms of microscopic deformation and microstructure evolution, is often represented by making use of constitutive modeling [12]. In recent years, various analytical, phenomenological, and empirical models have been developed to predict the constitutive behavior of a wide range of metals and alloys [13–16]. Among these models, the hyperbolic sine law in the Arrhenius equation has been widely applied for engineering applications. However, it lacks suitability for materials having obvious dynamic softening during hot deformation, since the influence of strain is not included. Accordingly, the researchers have put their efforts on the strain compensated Arrhenius model [17,18], and the prediction accuracy is greatly enhanced.

In the present study, hot deformation behavior and microstructure evolution of 2707 HDSS were investigated by conducting hot compression tests with varying deformation temperatures and strain rates. The effects of hot working parameters (strain rate and temperature) on the mechanical properties and microstructures were analyzed. Additionally, the experimentally measured true stress-strain curves were employed to establish a constitutive model using the strain compensated Arrhenius model. Moreover, the prediction accuracy of this model was evaluated by comparing the calculated and experimental flow stresses.

2. Experimental Procedures

The experimental 2707 HDSS was melted using a 25 kg vacuum induction melting furnace (Jinzhou Yuanteng Electric Furnace Technology Co., Ltd., Shenyang, China). The chemical composition (wt %) of the 2707 HDSS is as follows: 0.0044 C, 0.42 Si, 1.11 Mn, 26.83 Cr, 7.14 Ni, 4.88 Mo, 0.39 N, 0.97 Cu, 0.97 Co, 0.005 P, 0.003 S and Fe in balance. The ingot was forged into 110 mm × 30 mm billet in the temperature range of 1100–1200 °C. The cylindrical specimens with 8 mm diameter and 12 mm height were prepared from the hot forged billet with the longitudinal axis parallel to the deformation direction. A chromel-alumel thermocouple (Shenyang Dongda Sensor Technology Co., Ltd., Shenyang, China) was embedded in the middle of the specimen to monitor the temperature during hot compression. In order to reduce friction between the sample and thermal simulation testing machine squeeze head, graphite flakes with 0.25 mm thickness and 12 mm diameter were clamped between them. And tantalum sheets (Changsha Nanfang Tantalum Niobium Co., Ltd., Changsha, China) were used to prevent adhesion between the sample and the squeeze head [19].

Before the compression, all specimens were reheated to 1250 °C and held for 4 min to achieve homogenized microstructure. The microstructure of 2707 HDSS after reheating is exhibited in Figure 1, in which the volume fraction of ferrite and austenite is about 54% and 45%, respectively. Subsequently, the specimens were cooled to compression temperature at the rate of 5 °C/s and held for 30 s to eliminate temperature gradient. To investigate the effects of deformation temperature and strain rate, the uniaxial compression tests were performed on a Thermecmaster-Z tester (Fuji Electronic Industrial Co., Ltd., Tsurugashima, Japan) in the temperature range of 900–1250 °C with intervals of 50 °C and strain rate range of 0.01–10 s^{-1} with intervals of an order of magnitude, respectively. The specimens

were compressed up to a total strain of 0.8 followed by immediate quenching with forced gas to retain the deformed microstructure. Hot deformed specimens were cut along the longitudinal axis, mechanically ground, and polished. Following these steps, electrolytic etching in 10 wt % KOH solution was adopted to reveal microstructures. The microstructures of deformed specimens were characterized using an optical microscope (OM, Olympus Corporation, Tokyo, Japan) and scanning electron microscope (SEM, Japan Electron Optics Laboratory, Tokyo, Japan), and the composition of the constituents was analyzed using an energy dispersive spectroscope (EDS, Bruker, Berlin, Germany). In addition, a transmission electron microscope (TEM, FEI, Hillsboro, OR, USA) was used to confirm the precipitates and substructure.
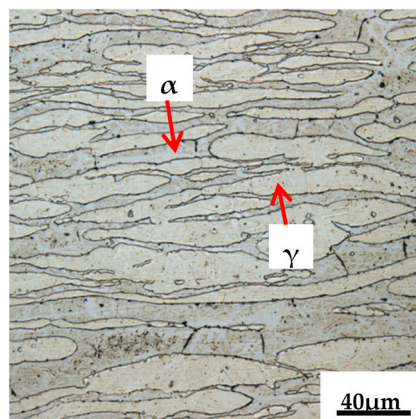

**Figure 1.** Optical microstructure of 2707 hyper duplex stainless steel (HDSS) after reheating.

3. Results and Discussions

3.1. Flow Stress-Strain Cures

The flow stress-strain curves of 2707 HDSS in the temperature range of 900–1250 °C and strain rate range of 0.01–10 s^{-1} are shown in Figure 2. Obviously, the flow stress was strongly dependent on both the deformation temperature and strain rate. Meanwhile, the peak stress increased with increasing strain rate and decreasing temperature. The results revealed that all the curves showed similar characteristics of work hardening at the early stage of deformation. The initial increment of stress as a result of work hardening is attributed to an increase of dislocation density [20].
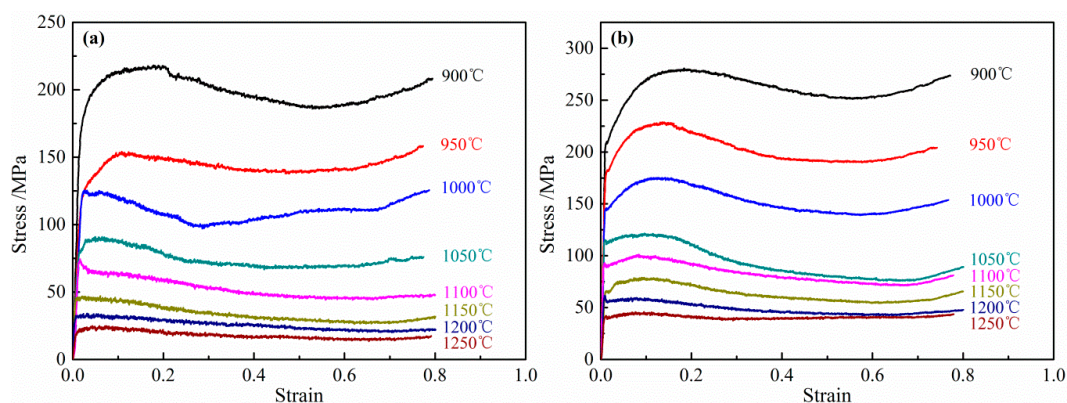

Figure 2. *Cont.*
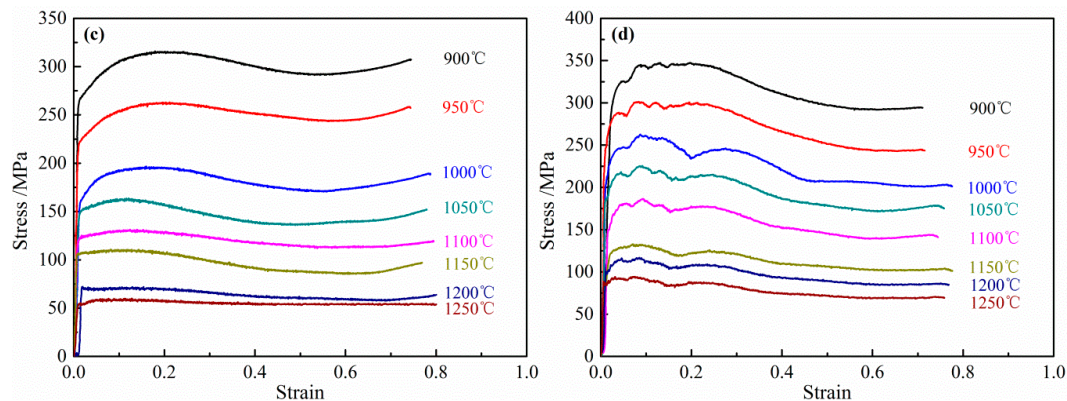
Figure 2. Flow stress vs. strain curves of 2707 HDSS under different strain rates: (**a**) 0.01 s^{-1}; (**b**) 0.1 s^{-1}; (**c**) 1 s^{-1}; (**d**) 10 s^{-1}.

After work hardening at the early stage of deformation, the curves presented different features in the different deformation conditions. The different features of flow curves can be interpreted considering the coexistence of different constituents, i.e., ferrite and austenite with different softening mechanisms and interaction of strain partitioning [21]. When the temperature was higher than 1100 °C and strain rate was less than 1 s^{-1}, the true stress-strain curves exhibited DRV characteristics without peak stress, as shown in Figure 2a–c. It could be explained that strain was mostly accommodated in ferrite because ferrite had higher SFE so that arrangement and annihilation of dislocations would occur more easily through DRV [22]. Flow curves with peak stress could be observed at lower temperatures, which may be attributed to the DRX or flow instability [23]. When strain rate was 10 s^{-1}, the flow curves exhibited significant waviness at strain lower than 0.2 as shown in Figure 2d, which was attributed to severely uneven distribution of strain in the ferrite and austenite phases at very high strain rates [24]. At the last stage of deformation, flow stress rose again because the effect of softening behavior was weaker than work hardening.

3.2. Analysis of Microstructure Evolution

The microstructures of 2707 HDSS under different deformation temperatures with strain of 0.8 and strain rate of 0.01 s^{-1} are shown in Figure 3. Figure 3a,b show that a large number of precipitates with the streamline shape appeared in ferrite and distributed along the deformation direction at 950 and 1050 °C. In order to identify the precipitates, SEM and TEM observation were performed as shown in Figures 4 and 5. SEM image shows that the ferrite was decomposed into one phase with coral-like structure and another phase with irregular island structure. And EDS analysis shows that the former phase was σ phase containing high content of Cr and Mo and the latter phase was secondary austenite with high Ni content, as reported by Paulraj et al. [25]. TEM image and selected area electron diffraction (SAED) pattern indicate σ phase with a tetragonal crystal structure presenting round type. The results of SEM and TEM analysis proved the occurrence of $\alpha \rightarrow \gamma_2 + \sigma$. It is reported that precipitates could restrain processing of discontinuous DRX because of precipitates pinning grain boundaries [26–29]. Therefore, it is difficult for discontinuous DRX to occur under these conditions. TEM image of the dislocation cells in ferrite is shown in Figure 6. The dislocation cells formed by tangled dislocations in ferrite indicate the occurrence of DRV in ferrite [30].
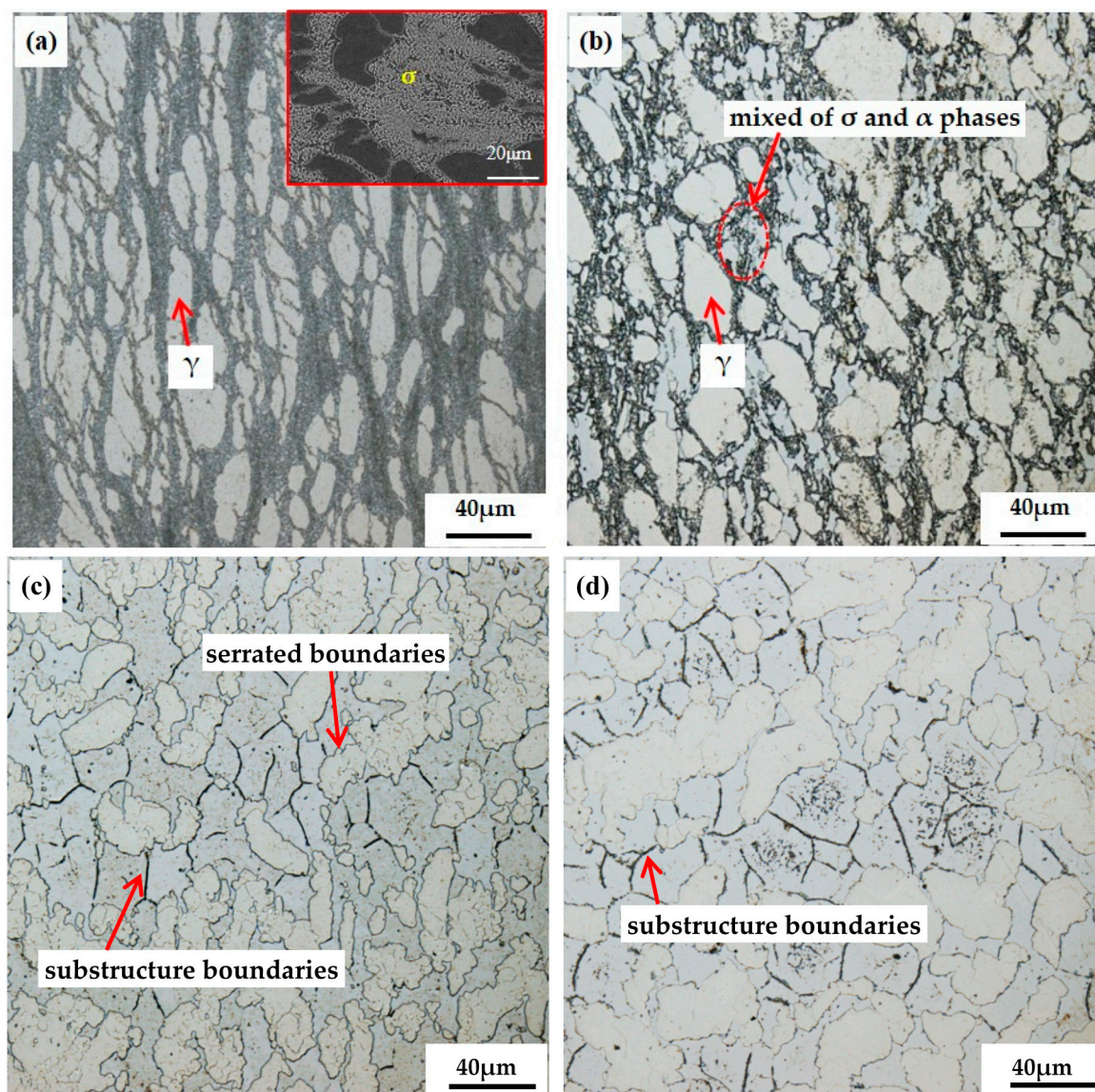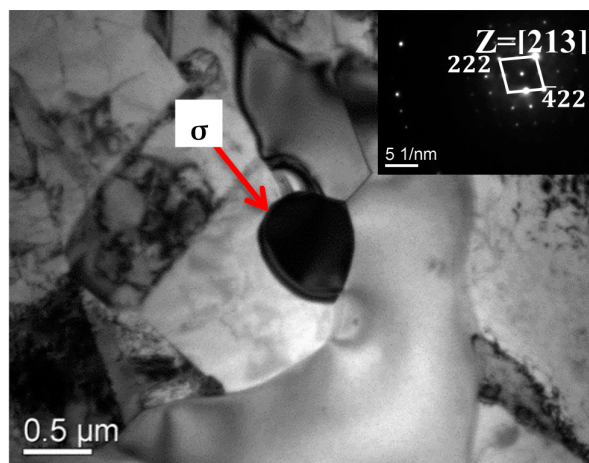
Figure 3. Microstructures of 2707 HDSS deformed at 0.01 s^{-1} and different temperatures: (**a**) 950 °C; (**b**) 1050 °C; (**c**) 1150 °C; (**d**) 1250 °C.

When the deformation temperature increased to 1150 °C, precipitates disappeared and a large amount of equiaxed ferrite appeared (Figure 3c). As indicated by arrows, sharper substructure in ferrite and some serrated boundaries in austenite were observed. It is considered that the leading softening mechanisms were DRV in ferrite and discontinuous DRX in austenite at the temperature of 1150 °C and strain rate of 0.01 s^{-1} [10,31]. When the deformation temperature reached 1250 °C, sharper substructure in ferrite indicated a well-developed DRV, as shown in Figure 3d. In addition, austenite had no obvious serrated boundaries and austenite islands became larger, indicating that strain was accumulated in the ferrite and did not spread to the austenite [32], and grain growth had occurred. These phenomena are consistent with the true stress-strain curves.
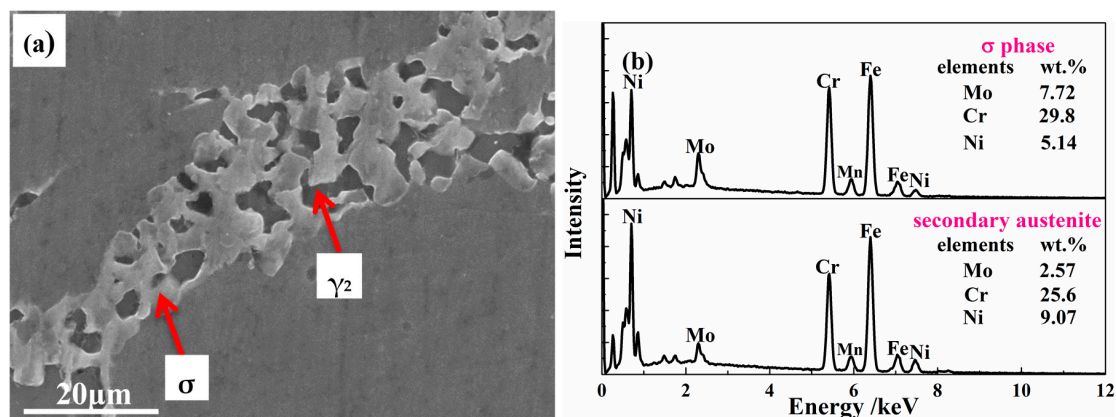
Figure 4. (**a**) SEM micrographs; and (**b**) energy dispersive spectroscope (EDS) analysis of precipitates and secondary austenite in 2707 HDSS deformed at 900 °C and 0.01 s^{-1}.

Figure 5. TEM micrograph and selected area electron diffraction (SAED) of σ in 2707 HDSS deformed at 900 °C and 0.01 s^{-1}.
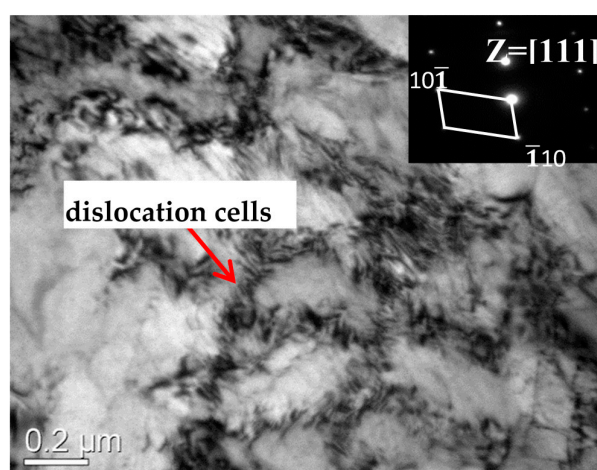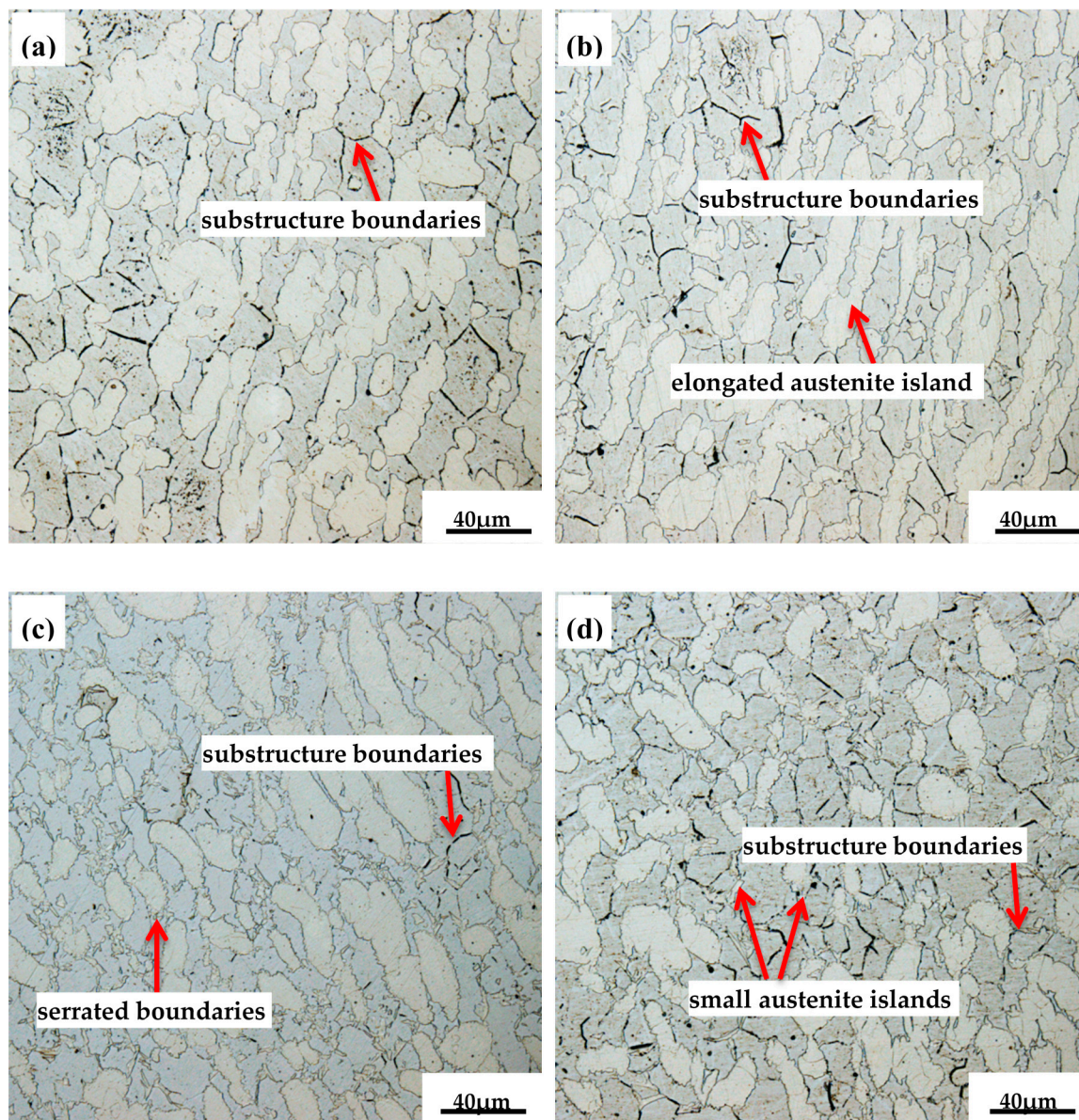

Figure 6. The dislocation cells in ferrite of 2707 HDSS deformed at 1050 °C and 0.01 s^{-1}.

Figure 7 shows the microstructures of 2707 HDSS deformed at 1250 °C and different strain rates. As shown in Figure 7a,b, the sharper substructure in ferrite can be observed. There were no obvious serrated boundaries in elongated austenite islands implying the restriction of discontinuous DRX.

Therefore, DRV in ferrite was the main softening mechanism. Consequently, strain was accumulated in the ferrite and did not spread to the austenite [32]. When the compression was conducted at 1 s^{-1}, a weak substructure in ferrite and serrated boundaries in austenite could be observed in Figure 7c. It indicted that the load was transformed from ferrite to austenite, leading to stain accumulation in austenite in latter stages triggering discontinuous DRX [33]. When the strain rate increased to 10 s^{-1}, the same phenomenon of discontinuous DRX could also be observed and the size of austenite islands was smaller because grains did not have enough time to grow, as shown in Figure 7d. A new DRX grain of austenite in 2707 HDSS, observed by TEM, is shown in Figure 8. The austenite developed into equiaxed grain and dislocation in the austenite interiors disappeared. Based on the above analysis, it could be concluded that the increase of strain rate was conducive to the occurrence of discontinuous DRX of austenite in 2707 HDSS.


Figure 7. Microstructures of 2707 HDSS deformed at 1250 °C and different strain rates: (**a**) 0.01 s^{-1}; (**b**) 0.1 s^{-1}; (**c**) 1 s^{-1}; (**d**) 10 s^{-1}.
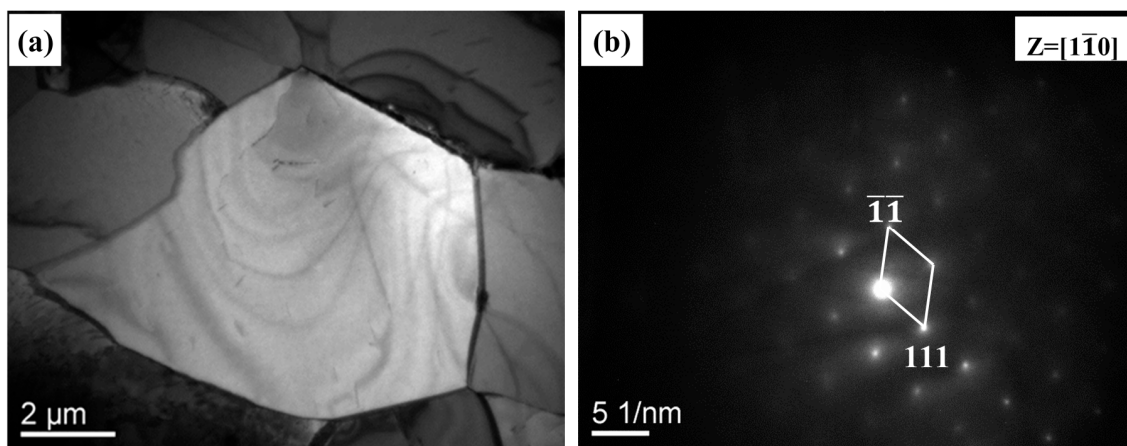
Figure 8. TEM images of specimens deformed at 1250 °C and 10 s^{-1}: (**a**) dynamic recrystallization (DRX) grain of austenite; (**b**) SAED result.

Besides, the existence of DRX grains in 2707 HDSS deformed at 1050 °C and 10 s^{-1} observed by TEM is shown in Figure 9. The new austenite grains were surrounded by dislocations, and the high dislocation density meant more significant plastic deformation characteristic [34]. However, discontinuous DRX phenomenon could not be observed, as shown in Figure 3b. From these, it could be concluded that the driving force of discontinuous DRX was the reduction of storage energy [35], and high strain rate could promote discontinuous DRX of austenite in 2707 HDSS.
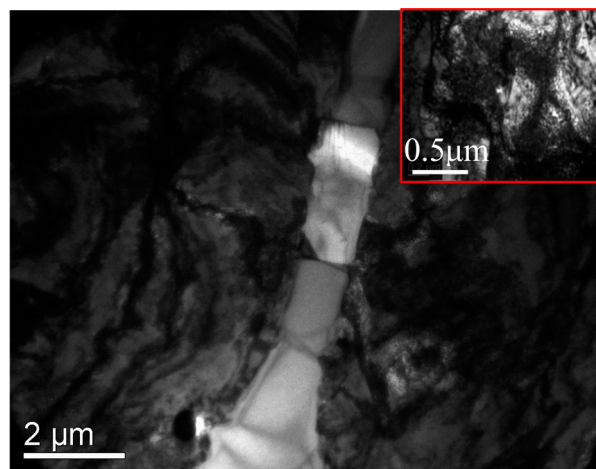
Figure 9. Dislocation structure around new DRX grains in 2707 HDSS deformed at 1050 °C and 10 s^{-1}.

In summary, all the curves showed similar characteristics of work hardening at the early stage of deformation. With the strain increasing, the curves presented different features in the different deformation conditions. At low temperatures, a large number of precipitates appeared in ferrite and distributed along the deformation direction, which could restrain processing of DRX and lead to flow instability. When the temperature increased, precipitates disappeared and the extent of DRV in ferrite enhanced, so the flow curves exhibited DRV characteristics without peak stress. Additionally, strain rate had important effects on the restoration process. At low strain rate, strain was accumulated in the ferrite and did not spread to the austenite, and DRV in ferrite was the main softening mechanism. When the strain rate increased to 1 s^{-1}, the load was transformed from ferrite to austenite, leading to strain accumulation in austenite in latter stages until the triggering of DRX. Consequently, the flow curves exhibited DRX characteristics with peak stress.

3.3. Establishment of Constitutive Relationship at Peak Strain

The constitutive equation is an important mathematical model to predict and analyze the relationship among temperature, strain rate, and flow stress in a wide hot deformation temperature range [36,37]. The dependence of flow stress to hot deformation variables can be analyzed by the well-known hyperbolic sine function [38] incorporated with the definition of the Zener-Hollomon parameter as follows:

$$Z = \dot{\varepsilon}\exp(Q/RT) \tag{1}$$

where Q, T, and R donate the apparent activation energy (J·mol^{-1}), absolute temperature (K), and universal gas constant (8.314 J·mol^{-1}·K^{-1}), respectively.

Based on the analysis of a large number of metals and alloys, many researchers have proposed the constitutive equations describing the thermal deformation of different metals and alloys [7,12,39,40]:

$$\dot{\varepsilon} = A_1\sigma^{n_1}\exp\left[-Q/(RT)\right] \tag{2}$$

$$\dot{\varepsilon} = A_2\exp(\beta\sigma)\exp\left[-Q/(RT)\right] \tag{3}$$

$$\dot{\varepsilon} = A\left[\sinh(\alpha\sigma)\right]^n\exp\left[-Q/(RT)\right] \tag{4}$$

where $\dot{\varepsilon}$ is the strain rate, σ is the flow stress, and A, A_1, A_2, n_1, n, β, and α (β/n_1) are material constants, respectively.

Taking the natural logarithm of Equations (2) and (3) yields:

$$\ln\dot{\varepsilon} = \ln A_1 + n_1\ln\sigma - Q/(RT) \tag{5}$$

$$\ln\dot{\varepsilon} = \ln A_2 + \beta\sigma - Q/(RT) \tag{6}$$

By plotting $\ln\dot{\varepsilon} - \sigma$ and $\ln\dot{\varepsilon} - \ln\sigma$, β and n_1 could be obtained from the slope of the linear regression lines, as shown in Figure 10a,b, respectively. The average value of n$_1$ and β were calculated to be 8.1803 and 0.0665, respectively, and then $\alpha = \beta/n_1 = 0.00813$ MPa^{-1}.

Taking the natural logarithm of Equation (4) yields:

$$\ln\dot{\varepsilon} = \ln A + n\ln\left[\sinh(\alpha\sigma)\right] - Q/(RT) \tag{7}$$

By plotting $\ln\dot{\varepsilon}$ against $\ln[\sinh(\alpha\sigma)]$ at constant temperatures, the material constant n can be calculated from the slope of the linear regression lines, as shown in Figure 10c. The average value of n was 5.514 based on the slope of four linear regression lines at different temperatures. Therefore, in the same way, the apparent activation energy (569.279 kJ·mol^{-1}) can be derived from the average slope of the $\ln[\sinh(\alpha\sigma)] - 1000/T$, as shown in Figure 10d. The value of A was 1.34×10^{21} in the present study based on the intercept of the $\ln Z - \ln[\sinh(\alpha\sigma)]$, as shown in Figure 10e. Filling the obtained material constants (α, n, Q, and A) into Equations (1) and (4), the hyperbolic sine equation embracing the Z parameter for the 2707 HDSS was developed as follows:

$$Z = \dot{\varepsilon}\exp(\frac{569279}{RT}) = 1.34 \times 10^{21}\left[\sinh(0.00813 \times \sigma)\right]^{5.514} \tag{8}$$
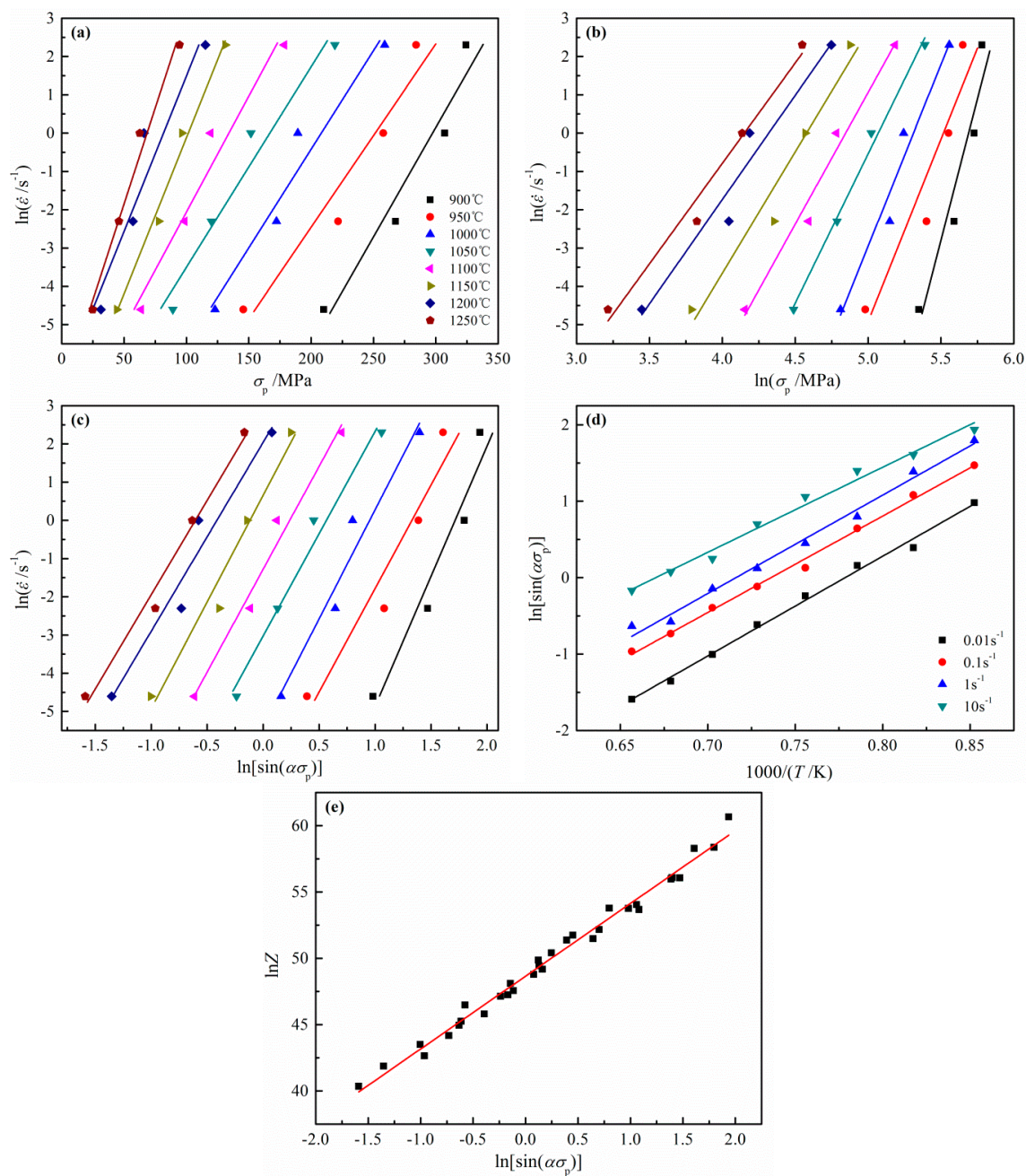
Figure 10. Relationships among flow strain rate and temperature for 2707 HDSS under hot compression: (**a**) $\ln\dot{\varepsilon} - \sigma$; (**b**) $\ln\dot{\varepsilon} - \ln\sigma$; (**c**) $\ln\dot{\varepsilon} - \ln[\sinh(\alpha\sigma)]$; (**d**) $\ln[\sinh(\alpha\sigma)] - 1000/T$; (**e**) $\ln Z - \ln[\sinh(\alpha\sigma)]$.

Many researchers [11,21,41] studied hot deformation activation energy of various typical DSSs, such as 2101, 2205 and 2507. In order to facilitate comparison, the content of main alloying elements and hot deformation activation energy of those steels reported in the literature are listed in Table 1.

Table 1. Chemical composition and apparent activation energy of duplex stainless steel (DSS)/wt %.

Steel Grades	C	Si	Mn	Cr	Ni	Mo	N	$Q/\text{kJ·mol}^{-1}$
as-21Cr EDSS [11]	0.02	0.58	4.65	21.03	1.26	0.03	0.24	401.6
2205 DSS [21]	0.023	0.001	1.35	22.07	4.83	2.37	0.19	460.9
2507 [41]	0.03	0.37	1.08	25.21	7.08	4.23	0.26	493.0
2707 HDSS	0.0044	0.42	1.11	26.83	7.14	4.88	0.37	569.279

It can be seen from Table 1 that hot deformation activation energy of 2707 HDSS is the highest among these DSSs. The *Q* value describes the activation barrier that atoms need to overcome during the deformation procedure [42]. It is generally believed that the higher alloy steels have higher strain activation energy. This is because of the solid solution strengthening effect of the alloying elements, the drag and drop effect of these solute atoms hindering slipping of dislocation, and the movement of the grain boundary [36]. Among the elements, Cr and Mo provide more contribution to thermal deformation activation energy [39]. Ni and N could also promote the value of *Q* [43]. In the present research, the content of Cr, Mo, Ni, and N were higher in 2707 HDSS than traditional DSSs, which increased hot deformation activation energy significantly.

3.4. Constitutive Modeling Considering Effect of Strain

It is considered that the effect of strain on flow stress at elevated temperature is insignificant and thus would usually be ignored in Equation (1) [44]. However, it could be found that the strain also has an important effect on the flow stress besides strain rate and deformation temperature as shown in Figure 2. Meanwhile, the effect of the strain on the material constants (i.e., α, β, n, Q, and $\ln A$) is significant in the entire strain range as shown in Figure 11. Therefore, compensation of strain should be taken into account in order to derive constitutive modeling to predict the flow stress more precisely. The effect of strain was represented by presuming that different material constants were polynomial functions of strain [45–47]. In the present study, the values of material constants of the constitutive relationships were calculated under various true strains within the range of 0.05–0.75 and the intervals of 0.05. The order of the fitted polynomial was varied from two to eight for selecting the best fitted model. As shown in Equation (9), a sixth order polynomial was found to represent the influence of strain on material constants with a good correlation and generalization, and the fitted curves are shown in Figure 11. A higher order (i.e. >6) polynomial would over-fit, thus losing the ability of true representation and generalization. The polynomial fit results of α, β, n, Q, and $\ln A$ of 2707 HDSS are provided in Table 2.

$$\alpha = \alpha_0 + \alpha_1 \varepsilon + \alpha_2 \varepsilon^2 + \alpha_3 \varepsilon^3 + \alpha_4 \varepsilon^4 + \alpha_5 \varepsilon^5 + \alpha_6 \varepsilon^6$$

$$\beta = \beta_0 + \beta_1 \varepsilon + \beta_2 \varepsilon^2 + \beta_3 \varepsilon^3 + \beta_4 \varepsilon^4 + \beta_5 \varepsilon^5 + \beta_6 \varepsilon^6$$

$$n = n_0 + n_1 \varepsilon + n_2 \varepsilon^2 + n_3 \varepsilon^3 + n_4 \varepsilon^4 + n_5 \varepsilon^5 + n_6 \varepsilon^6 \qquad (9)$$

$$Q = Q_0 + Q_1 \varepsilon + Q_2 \varepsilon^2 + Q_3 \varepsilon^3 + Q_4 \varepsilon^4 + Q_5 \varepsilon^5 + Q_6 \varepsilon^6$$

$$\ln A = A_0 + A_1 \varepsilon + A_2 \varepsilon^2 + A_3 \varepsilon^3 + A_4 \varepsilon^4 + A_5 \varepsilon^5 + A_6 \varepsilon^6$$

Table 2. Coefficients of the polynomial for α, β, n, Q, and $\ln A$ for 2707 HDSS.

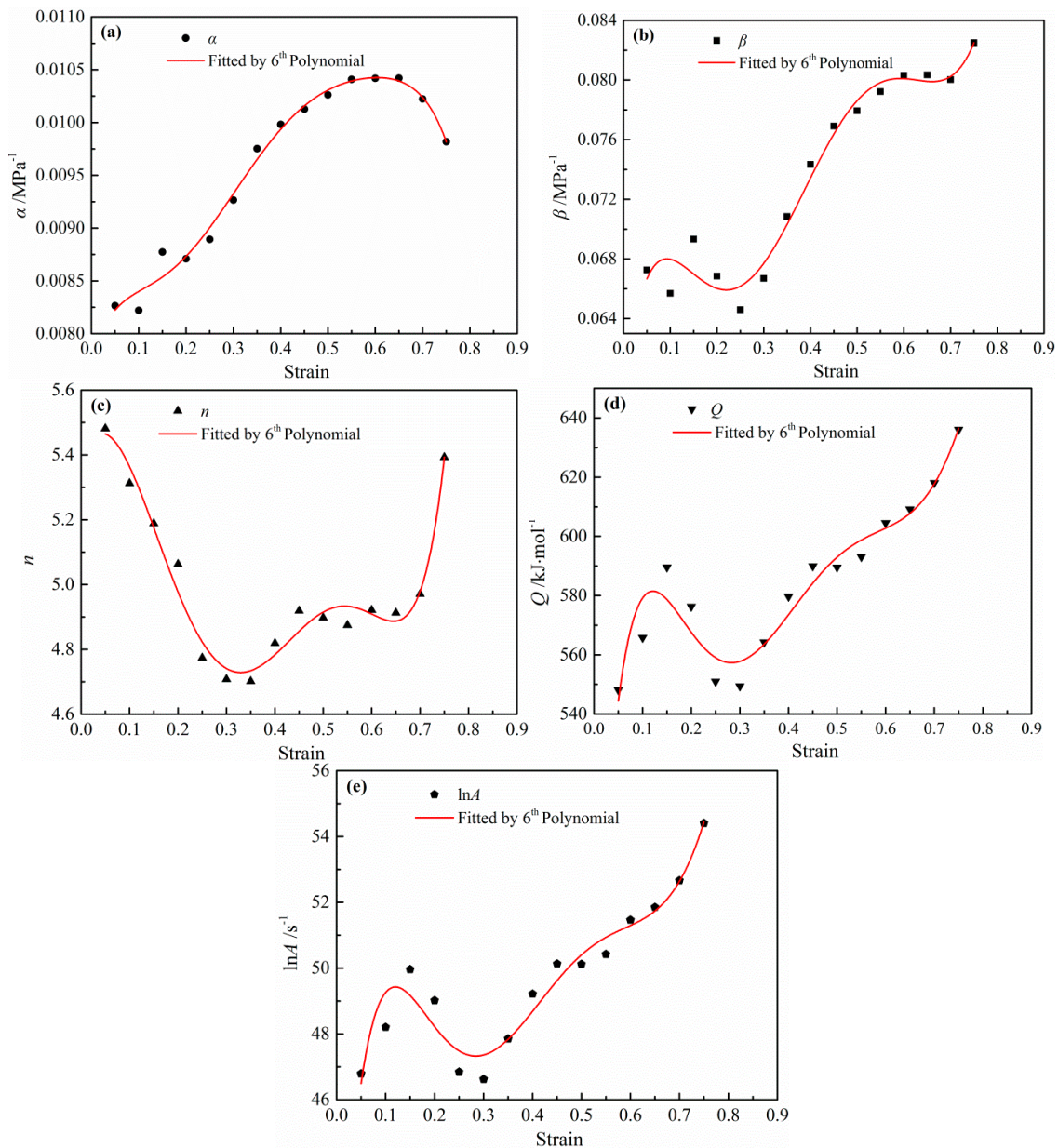| α	β	n	Q	$\ln A$
$\alpha_0 = 0.00778$	$\beta_0 = 0.05921$	$n_0 = 5.38072$	$Q_0 = 433.7134$	$A_0 = 37.6406$
$\alpha_1 = 0.01391$	$\beta_1 = 0.24588$	$n_1 = 4.23215$	$Q_1 = 3340.689$	$A_1 = 267.325$
$\alpha_2 = -0.13113$	$\beta_2 = -2.35617$	$n_2 = -58.3197$	$Q_2 = -26,985.42$	$A_2 = -2155.24$
$\alpha_3 = 0.68476$	$\beta_3 = 9.23339$	$n_3 = 145.989$	$Q_3 = 96,937.91$	$A_3 = 7660.88$
$\alpha_4 = -1.61171$	$\beta_4 = -16.0984$	$n_4 = 5.81170$	$Q_4 = -171,312.5$	$A_4 = -13,301.7$
$\alpha_5 = 1.76105$	$\beta_5 = 12.4872$	$n_5 = -350.183$	$Q_5 = 146,514.1$	$A_5 = 11,097.16$
$\alpha_6 = -0.73869$	$\beta_6 = -3.37538$	$n_6 = 277.087$	$Q_6 = -48,226.32$	$A_6 = -3528.39$

Figure 11. Relationship between material constants and strains: (**a**) α; (**b**) β; (**c**) *n*; (**d**) *Q*; (**e**) ln*A*.

Once the polynomial coefficients of all material constants were evaluated, the flow stress at a particular true strain can be estimated. Using the expression of hyperbolic sine function, the constitutive equation that relates to flow stress and the Zener-Holloman parameter can be written in the following form [48]:

$$\sigma = \frac{1}{\alpha}\ln\left\{\left(\frac{Z}{A}\right)^{\frac{1}{n}} + \left[\left(\frac{Z}{A}\right)^{\frac{2}{n}} + 1\right]^{\frac{1}{2}}\right\} \tag{10}$$

3.5. Verification of the Developed Constitutive Modeling

The experimental and calculated values were compared to evaluate the accuracy of the developed constitutive modeling in predicting the hot deformation behavior of 2707 HDSS, as illustrated in Figure 12. The calculated stress increased with increasing strain rate and decreasing deformation temperature. It can be observed that an agreement between the experimental and calculated values

is satisfactory for most of the experimental conditions. Only in some deformation conditions (i.e., at 900 °C in 0.1, 1, and 10 s^{-1}) was a notable deviation between experimental and calculated values observed. The fitting of material constants might result in the deviation between experimental and calculated values of flow stress. For example, as shown in Figure 10a, experimental data shows some aberration, particularly at the lower temperatures. Additionally, Equation (2) is suitable for lower stress as mentioned in a previous paragraph. Therefore, some errors might be introduced in calculating the values of n_1 using Equation (2) for higher stress (i.e., at lower temperature and higher strain rate) and finally affect the accuracy of constitutive modeling [44]. Similar errors were reported by Mandal et al. [48] in Ti-modified austenitic stainless steel and Zou et al. [12] in as-cast 21Cr economical duplex stainless steel.
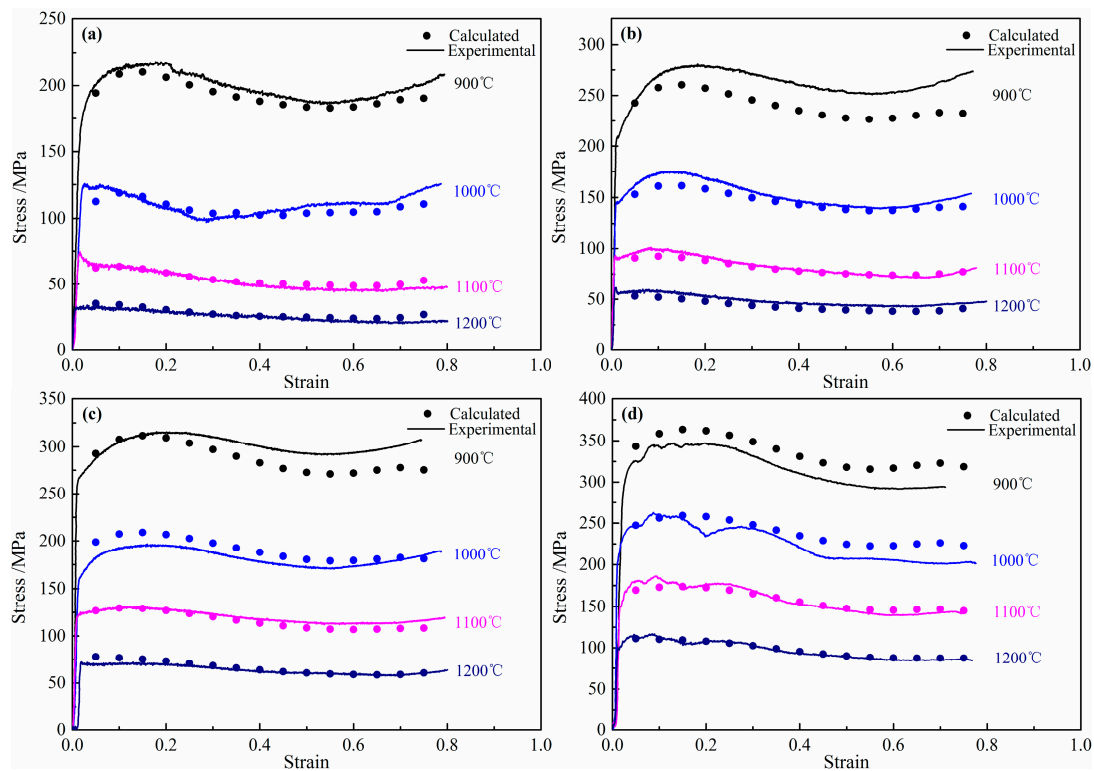
Figure 12. Comparison between calculated and experimental flow stress curves at strain rates: (**a**) 0.01 s^{-1}; (**b**) 0.1 s^{-1}; (**c**) 1 s^{-1}; (**d**) 10 s^{-1}.

With the aim to evaluate the accuracy of the developed constitutive modeling, standard statistical parameters such as correlation coefficient (R) and average absolute relative error (AARE) are adopted [7,44]. The parameters are expressed by the following equations:

$$R = \frac{\sum_{i=1}^{N} \left(E_i - \overline{E} \right)\left(P_i - \overline{P} \right)}{\sqrt{\sum_{i=1}^{N} \left(E_i - \overline{E} \right)^2 \left(P_i - \overline{P} \right)^2}} \tag{11}$$

$$AARE = \frac{1}{N} \sum_{i=1}^{N} \left| \frac{E_i - P_i}{E_i} \right| \times 100\% \tag{12}$$

where E_i is the experimental flow stress; P_i is the calculated flow stress; $\overline{E}$ and $\overline{P}$ are the mean values of E_i and P_i, respectively; N is the number of data points used in this investigation. The correlation coefficient R is used to reflect the strength of the linear relationship between the calculated and experimental values. Sometimes, higher values of R may not always indicate a better predictability and reliability because the tendency of the constitutive modeling could be biased towards higher or

lower values [49]. However, the AARE value is computed in terms of relative error and therefore is an impartial value for evaluating the capability of the modeling in the prediction of flow stress [47,50]. Figure 13 shows the plots of the calculated values of flow stress against the experimental values at various processing conditions. It is obvious that most of the data points lie very close to the line, and the correlation coefficient for the developed constitutive modeling of 2707 HDSS is 0.992. Meanwhile, the AARE value for the developed constitutive equation of 2707 HDSS alloy is 5.22%. These results show that the proposed constitutive modeling considering strain compensation provided a precise estimate of the flow stress of 2707 HDSS.
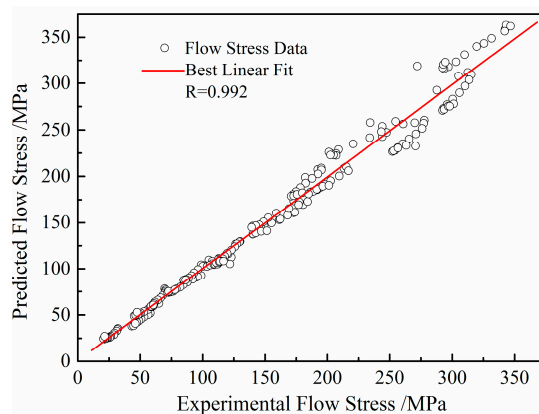
Figure 13. Correlation between the experimental and calculated flow stress data.

4. Conclusions

The hot deformation behavior, microstructure evolution, and constitutive analysis of 2707 HDSS were investigated by hot compression tests in the temperature range of 900–1250 °C and strain rate range of 0.01–10 s^{-1}. The main results are listed below:

(1) The flow stress was especially sensitive to deformation temperature and strain rate as it increased with increasing strain rate and decreasing deformation temperature. When the temperature was higher than 1100 °C and strain rate was less than 1 s^{-1}, the true stress-strain curves exhibited DRV characteristics without peak stress. Flow curves with peak stress could be observed at lower temperatures, which may be attributed to DRX or flow instability.

(2) At lower temperatures, a large number of precipitates appeared in ferrite and distributed along the deformation direction, which could restrain processing of discontinuous DRX because of pinning grain boundaries. When the temperature increased to 1150 °C, precipitates disappeared and sharper substructure in ferrite and some serrated boundaries in austenite were observed, indicating the leading softening behaviors were DRV in ferrite and discontinuous DRX in austenite. When the temperature reached 1250 °C, sharper substructure in ferrite and no obvious serrated boundaries in austenite showed that softening behavior was mainly DRV in ferrite. With the increasing of strain rate, the load was transformed from ferrite to austenite, leading to strain accumulation in austenite in latter stages until the triggering of discontinuous DRX.

(3) The peak stress of 2707 HDSS was well fitted by the constitutive modeling of the hyperbolic sine function. Due to the higher content of Cr, Mo, Ni, and N, 2707 HDSS processed higher apparent activation energy (569.279 kJ· mol^{-1}) than traditional DSSs.

(4) The hyperbolic sine constitutive model considering the compensation of strain was developed. A sixth order polynomial was found to be most suitable for describing the relationship between the material constants and the strains. The developed constitutive relationships of flow stress with strain, strain rate, and temperature were successfully used to predict the flow stresses under various deformation conditions, and the correlation coefficient and average absolute relative error were 0.992 and 5.22%, respectively.

Author Contributions: Huabing Li, Zhouhua Jiang, Lixin Wang, and Guangwei Fan conceived and designed the experiments; Weichao Jiao, Hao Feng, Xinxu Li, and Guoping Li performed the experiments; Weichao Jiao, Hao Feng, Xinxu Li, and Huabing Li analyzed the data; Huabing Li, Weichao Jiao, Xinxu Li, Hao Feng, and Peide Han contributed to the writing and editing of the manuscript.

Conflicts of Interest: The authors declare no conflict of interest.

References

1. Örnek, C.; Idris, S.A.M.; Reccagni, P.; Engelberg, D.L. Atmospheric-induced stress corrosion cracking of grade 2205 duplex stainless steel-effects of 475 °C embrittlement and process orientation. *Metals* **2016**, *6*, 167. [CrossRef]
2. Kim, S.K.; Kang, K.Y.; Kim, M.S.; Lee, J.M. Low-temperature mechanical behavior of super duplex stainless steel with sigma precipitation. *Metals* **2016**, *5*, 1732–1745. [CrossRef]
3. Zhao, H.; Zhang, Z.Y.; Zhang, H.Z.; Hu, J.; Li, J. Effect of aging time on intergranular corrosion behavior of a newly developed LDX 2404 lean duplex stainless steel. *J. Alloys Compd.* **2016**, *672*, 147–154. [CrossRef]
4. Li, H.B.; Zhou, E.Z.; Zhang, D.W.; Xu, D.K.; Xia, J.; Yang, C.; Feng, H.; Jiang, Z.H.; Li, X.G.; Gu, T.Y.; et al. Microbiologically influenced corrosion of 2707 hyper-duplex stainless steel by marine *pseudomonas aeruginosa* biofilm. *Sci. Rep.-UK* **2016**, *6*, 20190. [CrossRef] [PubMed]
5. Stenvall, P.; Holmquist, M. Weld properties of Sandvik SAF 2707. *Metall. Ital.* **2008**, *10*, 11–18.
6. Momeni, A.; Kazemi, S.; Bahrani, A. Hot deformation behavior of microstructural constituents in a duplex stainless steel during high-temperature straining. *Int. J. Miner. Metall. Mater.* **2013**, *20*, 953–960. [CrossRef]
7. Yang, L.C.; Pan, Y.T.; Chen, I.G.; Lin, D.Y. Constitutive relationship modeling and characterization of flow behavior under hot working for Fe–Cr–Ni–W–Cu–Co super-austenitic stainless steel. *Metals* **2015**, *5*, 1717–1731. [CrossRef]
8. Farnoush, H.; Momeni, A.; Dehghani, K.; Mohandesi, J.A.; Keshmiri, H. Hot deformation characteristics of 2205 duplex stainless steel based on the behavior of constituent phases. *Mater. Des.* **2010**, *31*, 220–226. [CrossRef]
9. Liu, Y.Y.; Yan, H.T.; Wang, X.H.; Yan, M. Effect of hot deformation mode on the microstructure evolution of lean duplex stainless steel 2101. *Mater. Sci. Eng. A* **2013**, *575*, 41–47. [CrossRef]
10. Momeni, A.; Dehghan, K. Hot working behavior of 2205 austenite–ferrite duplex stainless steel characterized by constitutive equations and processing maps. *Mater. Sci. Eng. A* **2011**, *528*, 1448–1454. [CrossRef]
11. Zou, D.N.; Wu, K.; Han, Y.; Zhang, W.; Cheng, B.; Qiao, G.J. Deformation characteristic and prediction of flow stress for as-cast 21Cr economical duplex stainless steel under hot compression. *Mater. Des.* **2013**, *51*, 975–982. [CrossRef]
12. Ashtiania, H.R.R.; Parsab, M.H.; Bisadia, H. Constitutive equations for elevated temperature flow behavior of commercial purity aluminum. *Mater. Sci. Eng. A* **2012**, *545*, 61–67. [CrossRef]
13. Abbasi-Bani, A.; Zarei-Hanzaki, A.; Pishbin, M.H.; Haghdadi, N. A comparative study on the capability of Johnson–Cook and Arrhenius-type constitutive equations to describe the flow behavior of Mg–6Al–1Zn alloy. *Mech. Mater.* **2014**, *71*, 52–61. [CrossRef]
14. Lin, Y.C.; Chen, X.M. A critical review of experimental results and constitutive descriptions for metals and alloys in hot working. *Mater. Des.* **2011**, *32*, 1733–1759. [CrossRef]
15. Haghdadi, N.; Zarei-Hanzaki, A.; Khalesian, A.R.; Abedi, H.R. Artificial neural network modeling to predict the hot deformation behavior of an A356 aluminum alloy. *Mater. Des.* **2013**, *49*, 389–361. [CrossRef]
16. Haghdadi, N.; Zarei-Hanzaki, A.; Abedi, H.R. The flow behavior modeling of cast A356 aluminum alloy at elevated temperatures considering the effect of strain. *Mat. Sci. Eng. A* **2012**, *535*, 252–257. [CrossRef]
17. Li, H.P.; He, L.F.; Zhao, G.Q.; Zhang, L. Constitutive relationships of hot stamping boron steel B1500HS based on the modified Arrhenius and Johnson–Cook model. *Mater. Sci. Eng. A* **2013**, *580*, 330–348. [CrossRef]
18. Lin, Y.C.; Xia, Y.C.; Chen, X.M.; Chen, M.S. Constitutive descriptions for hot compressed 2124-T851 aluminum alloy over a wide range of temperature and strain rate. *Comput. Mater. Sci.* **2010**, *50*, 227–233. [CrossRef]
19. Sun, C.Y.; Zuo, X.; Xiang, Y.; Yang, J. Investigation on hot deformation behavior and hot processing map of BSTMUF601 super-alloy. *Metals* **2016**, *70*, 1–8. [CrossRef]

20. Pu, E.X.; Feng, H.; Liu, M.; Zheng, W.J.; Dong, H.; Song, Z.G. Constitutive modeling for flow behaviors of super austenitic stainless steels S32654 during hot deformation. *J. Iron Steel Res. Int.* **2016**, *23*, 178–184. [CrossRef]

21. Yang, Y.H.; Yan, B. The microstructure and flow behavior of 2205 duplex stainless steels during high temperature compression deformation. *Mater. Sci. Eng. A* **2013**, *579*, 194–201. [CrossRef]

22. Haghdadi, N.; Martin, D.; Hodgson, P. Physically-based constitutive modelling of hot deformation behavior in a LDX 2101 duplex stainless steel. *Mater. Des.* **2016**, *106*, 420–427. [CrossRef]

23. Si, J.Y.; Liao, X.H.; Xie, L.Q.; Lin, K.H. Flow behavior and constitutive modeling of delta-processed Inconel 718 alloy. *J. Iron Steel Res. Int.* **2015**, *22*, 837–845. [CrossRef]

24. Han, Y.; Zou, D.N.; Chen, Z.Y.; Fan, G.W.; Zhang, W. Investigation on hot deformation behavior of 00Cr23Ni4N duplex stainless steel under medium–high strain rates. *Mater. Charact.* **2011**, *62*, 198–203. [CrossRef]

25. Paulraj, P.; Garg, R. Effect of intermetallic phases on corrosion behavior and mechanical properties of duplex stainless steel and super duplex stainless steel. *Adv. Sci. Technol. Res. J.* **2015**, *9*, 87–105. [CrossRef]

26. Doherty, R.D.; Hughes, D.A.; Humphreys, F.J.; Jonas, J.J.; Juul Jensen, D.; Kassner, M.E.; King, W.E.; McNelley, T.R.; McQueen, H.J.; Rollett, A.D. Current issues in recrystallization: A review. *Mater. Sci. Eng. A* **1997**, *238*, 219–274. [CrossRef]

27. Smith, C.S. Grains, phases, and interfaces—An interpretation of microstructure. *Trans. Metall. Soc. AIME* **1948**, *175*, 15–51.

28. Zurob, H.S.; Brechet, Y.; Purdy, G. A model for the competition of precipitation and recrystallization in deformed austenite. *Acta Mater.* **2001**, *49*, 4183–4190. [CrossRef]

29. Vervynckt, S.; Verbeken, K.; Thibauxc, P.; Houbaert, Y. Recrystallization–precipitation interaction during austenite hot deformation of a Nb microalloyed steel. *Mater. Sci. Eng. A* **2011**, *528*, 5519–5528. [CrossRef]

30. Timokhina, I.; Pereloma, E.V.; Hodgson, P. The formation of complex microstructures after different deformation modes in advanced high-strength steels. *Metall. Mater. Trans. A* **2014**, *45*, 4247–4256. [CrossRef]

31. Ma, X.C.; An, Z.J.; Chen, L.; Mao, T.Q.; Wang, J.F.; Long, H.J.; Xue, H.Y. The effect of rare earth alloying on the hot workability of duplex stainless steel—A study using processing map. *Mater. Des.* **2015**, *86*, 848–854. [CrossRef]

32. Balancin, O.; Hoffmann, W.A.M.; Jonas, J.J. Influence of microstructure on the flow behavior of duplex stainless steels at high temperatures. *Metall. Mater. Trans. A* **2000**, *31*, 1353–1364. [CrossRef]

33. Tehovnik, F.; Arzenšek, B.; Arh, B.; Skobir, D.; Pirnar, B.; Žužek, B. Microstructure evolution in SAF 2507 super duplex stainless steel. *Mater. Technol.* **2011**, *45*, 339–345.

34. Ma, M.; Ding, H.; Tang, Z.Y.; Zhao, J.T.; Jiang, Z.H.; Li, G. Effect of strain rate and temperature on hot workability and flow behaviour of duplex stainless steel. *Ironmak. Steelmak.* **2016**, *43*, 88–96. [CrossRef]

35. Wang, S.L.; Zhang, M.X.; Wu, H.C.; Yang, B. Study on the dynamic recrystallization model and mechanism of nuclear grade 316LN austenitic stainless steel. *Mater. Charact.* **2016**, *118*, 92–101. [CrossRef]

36. Xi, T.; Yang, C.G.; Shahzad, M.B.; Yang, K. Study of the processing map and hot deformation behavior of a Cu-bearing 317LN austenitic stainless steel. *Mater. Des.* **2015**, *87*, 303–312. [CrossRef]

37. Sun, C.Y.; Xiang, Y.; Zhou, Q.J.; Politis, D.J.; Sun, Z.H.; Wang, M.Q. Dynamic recrystallization and hot workability of 316LN stainless steel. *Metals* **2016**, *6*, 152. [CrossRef]

38. McQueen, H.J.; Ryan, N.D. Constitutive analysis in hot working. *Mater. Sci. Eng. A* **2002**, *322*, 43–63. [CrossRef]

39. McQueen, H.J.; Yue, A.S.; Ryan, N.D.; Fry, E. Hot working characteristics of steels in austenitic state. *J. Mater. Process. Technol.* **1995**, *53*, 293–310. [CrossRef]

40. Zener, C.; Hollomon, J.H. Effect of strain rate upon plastic flow of steel. *J. Appl. Phys.* **1944**, *22*, 22–32. [CrossRef]

41. Ma, M.; Ding, H.; Tang, Z.Y.; Zhao, J.W.; Jiang, Z.H.; Fan, G.W. Effects of temperature and strain rate on flow behavior and microstructural evolution of super duplex stainless steel under hot deformation. *J. Iron Steel Res. Int.* **2016**, *23*, 244–252. [CrossRef]

42. Farabi, E.; Zarei-Hanzaki, A.; Pishbin, M.H.; Moallemi, M. Rationalization of duplex brass hot deformation behavior: The role of microstructural components. *Mater. Sci. Eng. A* **2015**, *641*, 360–368. [CrossRef]

43. Pu, E.X.; Zheng, W.J.; Xiang, J.Z.; Song, Z.G.; Li, J. Hot deformation characteristic and processing map of superaustenitic stainless steel S32654. *Mater. Sci. Eng. A* **2014**, *598*, 174–182. [CrossRef]

44. Cai, J.; Li, F.G.; Liu, T.Y.; Chen, B.; He, M. Constitutive equations for elevated temperature flow stress of Ti–6Al–4V alloy considering the effect of strain. *Mater. Des.* **2011**, *32*, 1144–1151. [CrossRef]

45. Samantaray, D.; Mandal, S.; Bhaduri, A.K. Constitutive analysis to predict high-temperature flow stress in modified 9Cr–1Mo (P91) steel. *Mater. Des.* **2010**, *31*, 981–984. [CrossRef]

46. Lin, Y.C.; Chen, M.S.; Zhong, J. Constitutive modeling for elevated temperature flow behavior of 42CrMo steel. *Comput. Mater. Sci.* **2008**, *42*, 470–477. [CrossRef]

47. Mandal, S.; Rakesh, V.; Sivaprasad, P.V.; Venugopal, S.; Kasiviswanathan, K.V. Constitutive equations to predict high temperature flow stress in a Ti-modified austenitic stainless steel. *Mater. Sci. Eng. A* **2009**, *500*, 114–121. [CrossRef]

48. Li, H.Y.; Wei, D.D.; Hu, J.D.; Li, Y.H.; Chen, S.L. Constitutive modeling for hot deformation behavior of T24 ferritic steel. *Comput. Mater. Sci.* **2012**, *53*, 425–430. [CrossRef]

49. Phaniraj, M.P.; Lahiri, A.K. The applicability of neural network model to predict flow stress for carbon steels. *J. Mater. Process. Technol.* **2003**, *141*, 219–227. [CrossRef]

50. Xiao, M.L.; Li, F.G.; Zhao, W.; Yang, G.L. Constitutive equation for elevated temperature flow behavior of TiNiNb alloy based on orthogonal analysis. *Mater. Des.* **2012**, *35*, 184–193. [CrossRef]